# Elastohydrodynamic lubrication and finite configuration changes in reciprocating elastomeric seals

Stanisław Stupkiewicz *, Artur Marciniszyn

*Institute of Fundamental Technological Research (IPPT), Świętokrzyska 21, 00–049 Warsaw, Poland*

**Abstract**

A computational framework has been developed for a fully coupled analysis of elastohydrodynamic lubrication and finite deformations of elastomeric reciprocating seals in hydraulic actuators. The relevant formulation is provided, which consistently treats finite configuration changes of the seal modelled as a hyperelastic (Mooney-Rivlin) solid. The steady-state hydrodynamic lubrication is modelled using the classical Reynolds equation. Coupling of the solid and fluid parts is fully accounted for, including friction due to shear stresses in the lubricant film. Detailed results of finite element simulations are provided for two benchmark problems of O-ring and rectangular rod seals in a wide range of process parameters.

*Key words:* Elastohydrodynamic lubrication, Hyperelastic model, Dynamic sealing

## 1 Introduction

Hydrodynamic lubrication in reciprocating hydraulic seals is a classical topic studied experimentally and theoretically for more than 50 years now, cf. Nau [1]. It is thus rather surprising that detailed solutions of the corresponding elastohydrodynamic lubrication problems are not easily found in the literature, particularly in view of the substantial progress in computational techniques and increase of computer power observed in the last decades. This paper aims at filling this gap by providing the relevant formulation, which consistently treats finite configuration changes, along with a computational scheme and detailed results of numerical simulations.

* Corresponding author.
*Email address:* sstupkie@ippt.gov.pl (Stanisław Stupkiewicz).

Compared to the more classical hard EHL problems [2], in the soft EHL problems of elastomeric seals, the lubricant pressures are relatively low so that effects such as variation of viscosity with pressure and compressibility of the fluid are not essential. At the same time, in the case of hard EHL problems, the maximum pressure is typically two orders of magnitude smaller than the elastic modulus and thus the linear elasticity is an appropriate model for contacting members. This is not the case of elastomeric seals which are characterized by a very low elastic stiffness so that the lubricant pressures may easily exceed the shear modulus by one order of magnitude. Accordingly, finite deformations with finite configuration changes are expected to occur, at least locally, and these require appropriate theoretical and numerical treatment.

Simulation of the hydrodynamic lubrication in the seal-rod system requires determination of the flow of the lubricant (hydraulic fluid) in the thin film between the seal and the rod and, in parallel, determination of the deformation of the seal. Clearly, the two phenomena are coupled, and several available solution methods differ in the way in which this coupling is treated.

The inverse hydrodynamic theory (cf. Müller and Nau [3]) is based on the assumption that the contact pressure is not affected by the lubricating film developing between the seal and the rod (as the film thickness is much smaller than the elastic deflections of the seal). Accordingly, the distribution of the contact pressure, obtained from a purely mechanical contact analysis, is used to estimate the film thickness in characteristic points along the contact interface. Here, and in all the other relevant models, the fluid part is conveniently described by the Reynolds equation.

In the elastohydrodynamic lubrication problem, the elastic deflections of the seal are solved simultaneously with the Reynolds equation. In the early works, the linear elasticity together with the finite element method were used for that purpose, typically combined with the static condensation, cf. Ruskell [4], Yang and Hughes [5]. Prati and Strozzi [6] developed a model based on the finite-deformation theory with a hyperelastic material model adopted for the seal. The corresponding finite element model was used to compute the contact pressures while the (linear) influence coefficient matrix obtained through the nodal perturbation technique was used in the EHL analysis. Influence coefficients were also used by Salant et al. [7].

Simplified analytical models have been developed for rectangular seals, which have particularly simple geometry, cf. Field and Nau [8]. Similar approach has been used in a recent model of Nikas [9] which has also been extended to account for nonlinear elasticity of elastomeric seals, cf. Nikas and Sayles [10]. However, these simplified models are not able to represent some features of the solution, for instance, the pressure peaks at the rounded corners which were observed experimentally and also were predicted numerically by Prati

and Strozzi [6], see also Section 4.2.

In the present approach, the nonlinearities associated with the finite configuration changes and hyperelasticity of the seal are fully accounted for. The focus of this work is on the coupling of the hydrodynamic lubrication and finite deformations of the seal. Accordingly, several effects, such as the influence of surface roughness (e.g. Nikas [9], Salant et al. [7]) and extrusion of the seal at the air side, which are known to be important in some situations, are not addressed here. Also, to fix the attention, the rod seals are only referred to throughout the paper, although, the approach is obviously more general.

The formulation of the corresponding EHL problem is introduced in Section 2 and the finite element discretization along with the adopted solution strategy are discussed in Section 3. As an application, the analysis of the steady-state hydrodynamic lubrication and dynamic sealing performance of reciprocating O-ring and rectangular seals is carried out in Section 4. Due to the simple geometry, these two types of seals are particularly suitable for benchmark and verification examples. Based on the study of convergence of the solution with mesh refinement, relatively fine discretization has been used for the computations. Accordingly, fine features of the solutions could be captured, such as sharp minima and maxima of the film thickness and pressure at the outlet and inlet zones. Results of similar scope could not be found in the literature.

## 2 Problem formulation

### *2.1 Finite deformations of hyperelastic seal*

The present model of the seal–rod system accounts for the deformations of the seal due to the action of the hydrostatic sealed pressure as well as contact interactions with the housing and with the rod, the latter in the hydrodynamic lubrication regime. The housing and the rod are assumed rigid, while the elastomeric seal will typically undergo finite deformations, at least locally. Accordingly, two configurations are introduced, the stress-free initial (reference) configuration $\Omega$ and the deformed configuration $\omega$, as illustrated in Fig. 1. The boundary $\partial\Omega$ is divided [1] into three parts $\partial_l\Omega$, $\partial_p\Omega$ and $\partial_c\Omega$ associated with the hydrodynamic lubrication, hydrostatic sealed pressure and contact interaction

[1] There is no exact criterion for the transition from hydrostatic pressure loading on $\partial_p\Omega$ to hydrodynamic conditions on $\partial_l\Omega$. However, in practice, the transition point can be chosen arbitrarily provided that the film thickness at this point is much higher than the thickness in the actual lubrication zone (see also the discussion following Eqs. (17)–(18) in the next subsection). Similar argument applies for the boundary between $\partial_l\Omega$ and $\partial_c\Omega$ at the air side.

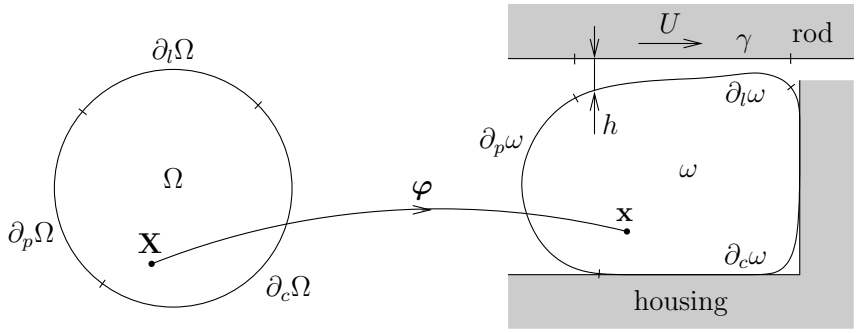


Fig. 1. Rod seal: initial (reference) and deformed configurations.

with the housing, respectively. The deformed-configuration counterparts are $\partial_l\omega$, $\partial_p\omega$ and $\partial_c\omega$, cf. Fig. 1.

The deformation from $\Omega$ to $\omega$ is described by a continuous mapping $\mathbf{x} = \boldsymbol{\varphi}(\mathbf{X})$, where $\mathbf{X} \in \Omega$ and $\mathbf{x} \in \omega$, and the deformation gradient $\mathbf{F} = \operatorname{Grad} \boldsymbol{\varphi}$ is the basic strain-like variable. In the absence of body and inertia forces, the weak form of the equilibrium equation is given by

$$\int_\Omega \mathbf{P} \cdot \operatorname{Grad} \delta\boldsymbol{\varphi} \, \mathrm{d}V - \int_{\partial\Omega} \mathbf{T} \cdot \delta\boldsymbol{\varphi} \, \mathrm{d}S = 0, \tag{1}$$

where $\mathbf{P}$ is the first Piola–Kirchhoff stress tensor and $\mathbf{T}$ is the *nominal* traction vector prescribed on the boundary $\partial\Omega$ (the nominal traction is referred to the unit area in the reference configuration).

The constitutive law of a hyperelastic material is fully defined by the elastic strain energy function $W(\mathbf{F})$, namely

$$\mathbf{P} = \frac{\partial W}{\partial \mathbf{F}}. \tag{2}$$

In this work, the Mooney-Rivlin material model is used, for which the strain energy function can be written as

$$W(\mathbf{F}) = \frac{1}{2}\,\mu_1(\bar{I}_1 - 3) + \frac{1}{2}\,\mu_2(\bar{I}_2 - 3) + W_v(I_3), \tag{3}$$

where $\bar{I}_1$, $\bar{I}_2$ and $I_3$ are the invariants of the left Cauchy-Green deformation tensor $\mathbf{B}$,

$$\bar{I}_1 = \operatorname{tr} \bar{\mathbf{B}}, \qquad \bar{I}_2 = \frac{1}{2}(\bar{I}_1^2 - \operatorname{tr} \bar{\mathbf{B}}^2), \qquad I_3 = \det \mathbf{B}, \tag{4}$$

and

$$\mathbf{B} = \mathbf{F}\mathbf{F}^T, \qquad \bar{\mathbf{B}} = I_3^{-1/3}\mathbf{B}. \tag{5}$$

Here $\mu_1$ and $\mu_2$ are material parameters such that $\mu = \mu_1 + \mu_2$ is the shear modulus in the initial configuration. With $\kappa$ denoting the bulk modulus, the volumetric part $W_v(I_3)$ is given by

$$W_v(I_3) = \frac{1}{2}\,\kappa\left(\frac{1}{2}(I_3 - 1) - \frac{1}{2}\log I_3\right). \tag{6}$$

The surface traction term in Eq. (1) can be equivalently evaluated in the deformed configuration, namely

$$\int_{\partial\Omega} \mathbf{T}\cdot\delta\boldsymbol{\varphi}\,\mathrm{d}S = \int_{\partial\omega} \mathbf{t}\cdot\delta\boldsymbol{\varphi}\,\mathrm{d}s, \tag{7}$$

where $\mathbf{t}$ is the *spatial* traction vector, i.e. one referred to the unit area in the deformed configuration. The later form is more convenient in the case of the hydrostatic and hydrodynamic pressure loading. The integrals in Eq. (7) are thus split into three parts corresponding to $\partial_p\omega$, $\partial_l\omega$ and $\partial_c\omega$. On $\partial_p\omega$, the spatial traction is given by

$$\mathbf{t} = -p_s\mathbf{n} \qquad \text{on } \partial_p\omega, \tag{8}$$

where $p_s$ is the sealed pressure and $\mathbf{n}$ is the unit vector normal to the surface in the deformed configuration and pointing outward. The loading from the hydrodynamic pressure along the lubricated boundary $\partial_l\omega$ is treated analogously, as discussed in more detail in Section 2.2.

Finally, the contribution from unilateral frictionless contact with the housing along the contact boundary $\partial_c\omega$ is introduced in a standard manner using Lagrange multipliers (e.g. Wriggers [11]), so that

$$\int_{\partial_c\omega} \mathbf{t}\cdot\delta\boldsymbol{\varphi}\,\mathrm{d}s = \int_{\partial_c\omega} \lambda_N\delta g_N\,\mathrm{d}s, \tag{9}$$

where the Lagrange multipliers $\lambda_N$ and the normal gap $g_N$ (defined such that $g_N > 0$ in case of separation) satisfy the Signorini condition,

$$g_N \geq 0, \quad \lambda_N \leq 0, \quad g_N\lambda_N = 0 \qquad \text{on } \partial_c\omega. \tag{10}$$

In our implementation, the unilateral contact conditions (10) are regularized using the augmented Lagrangian technique, cf. Alart and Curnier [12], but

other approaches could also used. Details of the treatment of the unilateral contact interactions are not discussed here.

### *2.2 Reynolds equation*

The flow of the lubricant (hydraulic fluid) in the thin gap between two solids in relative motion can be described by the well-known Reynolds equation, cf. Dowson and Higginson [2], Müller and Nau [3]. The basic assumption of the Reynolds equation is that the lubricant film thickness is small compared to the other dimensions of the domain. It is thus formulated on the nominal contact surface, which is assumed to approximately coincide with the two contacting surfaces. As in our case the elastomeric seal undergoes finite configuration changes, it must be explicitly stated that the Reynolds equation and all the quantities involved refer to the lubricated boundary $\partial_l\omega$ in the *deformed* configuration.

Let us thus introduce the nominal contact surface $\gamma$ as the domain in which the Reynolds equation holds. To fix the attention, $\gamma$ can be identified with the projection of the deformed boundary $\partial_l\omega$ onto the rigid surface of the rod. For incompressible fluid, the Reynolds equation can now be written in the form

$$\operatorname{div}_\gamma \mathbf{q} + \frac{\partial h}{\partial t} = 0, \qquad \mathbf{q} = \bar{\mathbf{u}} h - \frac{h^3}{12\eta} \operatorname{grad}_\gamma p, \tag{11}$$

where $p$ is the pressure, $h$ the film thickness, $\mathbf{q}$ the lubricant flux, $\bar{\mathbf{u}}$ the average velocity of the contacting surfaces, and $\eta$ the viscosity. These quantities are defined on the domain $\gamma$, hence the subscript in the operators denoting the divergence and gradient within $\gamma$. The dependence of viscosity on pressure is accounted for by adopting the classical Barus equation,

$$\eta = \eta_0 \exp(\alpha p), \tag{12}$$

where $\alpha$ is the pressure-viscosity coefficient and $\eta_0$ is the viscosity at zero pressure.

The essential and the natural boundary conditions are enforced on the parts of the boundary of $\gamma$, respectively, $\partial_p\gamma$ and $\partial_q\gamma$. Denoting the prescribed pressure by $p^*$ and the prescribed flux by $q_n^*$ we have

$$p = p^* \quad \text{on } \partial_p\gamma, \qquad \mathbf{q} \cdot \mathbf{n}_\gamma = q_n^* \quad \text{on } \partial_q\gamma. \tag{13}$$

The weak form of the Reynolds equation, which constitutes the basis of the finite element formulation, is obtained in a standard manner by multiplying

Eq. (11) by the test function $\delta p$, which vanishes on $\partial_p\gamma$, and integrating over the domain $\gamma$. Application of the Gauss theorem leads to the following weak form,

$$\int_\gamma \left( \mathrm{grad}_\gamma \delta p \cdot \mathbf{q} - \delta p \frac{\partial h}{\partial t} \right) \mathrm{d}\gamma - \int_{\partial_q\gamma} \delta p q_n^* \mathrm{d}l = 0. \tag{14}$$

In the case considered in this work, the Reynolds equation simplifies significantly. Firstly, the axial symmetry is assumed in the examples, so that the Reynolds equation becomes one-dimensional with, say, $\xi$ as the only spatial variable involved (here $\xi$ is a local coordinate which parameterizes $\gamma$). Secondly, in steady-state conditions, the term $\partial h/\partial t$ vanishes. Finally, only the essential boundary conditions are considered, namely conditions $p(\xi^-) = p_s$ and $p(\xi^+) = 0$ are enforced on the sealed-pressure side and on the air side, respectively. The corresponding one-dimensional weak form reads

$$\int_{\xi^-}^{\xi^+} \frac{\mathrm{d}\delta p}{\mathrm{d}\xi} \left( \bar{u}h - \frac{h^3}{12\eta} \frac{\mathrm{d}p}{\mathrm{d}\xi} \right) \mathrm{d}\xi = 0, \tag{15}$$

where $\bar{u} = U/2$ and $U$ is the rod speed (positive for outstroke, as indicated in Fig. 1).

In order to avoid a non-physical pressure drop below zero in the outlet zone, the cavitation condition $p \geq 0$ is approximately enforced using the penalty method, cf. Wu [13]. The corresponding weak form becomes then

$$\int_{\xi^-}^{\xi^+} \left[ \frac{\mathrm{d}\delta p}{\mathrm{d}\xi} \left( \bar{u}h - \frac{h^3}{12\eta} \frac{\mathrm{d}p}{\mathrm{d}\xi} \right) + \epsilon \delta p \max(-p, 0) \right] \mathrm{d}\xi = 0, \tag{16}$$

where $\epsilon > 0$ is a cavitation penalty parameter. The penalty term has no effect in the region of positive pressure and, at the same time, it penalizes the negative pressures which tend to zero for sufficiently large $\epsilon$. This approach is simple and straightforward in implementation and proves sufficient for the range of problems addressed in this work.

The coupling of the Reynolds equation (16) and the equilibrium equation (1) is through the dependence of the film thickness $h$ on the deformation of the seal and, secondly, through the forces exerted by the fluid on the seal boundary $\partial_l\omega$. The corresponding surface traction is given by

$$\mathbf{t} = -p\mathbf{n} + \tau\mathbf{s} \qquad \text{on } \partial_l\omega, \tag{17}$$

where the first term is due to the hydrodynamic pressure $p$ and the second term is due to the shear stress [2] $\tau$,

$$\tau = \frac{\eta U}{h} - \frac{h}{2}\frac{\mathrm{d}p}{\mathrm{d}\xi}, \tag{18}$$

which follows from the parabolic velocity profile across the film as assumed by the Reynolds equation. The unit vector $\mathbf{s}$ in Eq. (17) is constant and tangent to the nominal surface $\gamma$. At the same time, the hydrodynamic pressure loading is assumed to follow the current normal to the deformed surface. Accordingly, the hydrostatic and hydrodynamic pressure loading along, respectively, $\partial_p\omega$ and $\partial_l\omega$, are treated consistently.

As already mentioned in the previous subsection, there is quite some freedom in choosing the point of transition from hydrostatic to hydrodynamic conditions (i.e. the boundary between $\partial_p\omega$ and $\partial_l\omega$ at the sealed-pressure side and between $\partial_c\omega$ and $\partial_l\omega$ at the air side). This is because of the second term in the expression $(11)_2$ defining the lubricant flux, which is cubic in $h$. Thus, as the film thickness $h$ increases in the inlet and outlet zones, the pressure gradient quickly converges to zero. Accordingly, the position at which the essential boundary condition $(13)_1$ is enforced has a negligible effect on the solution of the Reynolds equation, provided that this point is sufficiently far from the actual hydrodynamic lubrication region (i.e. region of small film thickness). In practice, this requires that an initial contact analysis is performed in order to determine a suitable position of the transition point.

## 3 Numerical treatment

### *3.1 Finite element discretization*

The finite element method is used to solve the elastohydrodynamic lubrication problem defined in the previous section. Recall that the problem is specified by the mechanical equilibrium equation (the solid part) and the Reynolds equation (lubrication), expressed by the respective variational weak forms (1) and (14). The virtual work of surface tractions, i.e. the second term in Eq. (1), is further split into three parts corresponding to the hydrostatic pressure on $\partial_p\omega$, contact with the housing on $\partial_c\omega$, and hydrodynamic lubrication on $\partial_l\omega$.

[2] Note that the effect of friction on the deformation of the contacting bodies is usually assumed negligible in EHL problems. This assumption is only partially justified in the present case of elastometric seals (soft EHL problems), as illustrated by the numerical examples in Section 4.

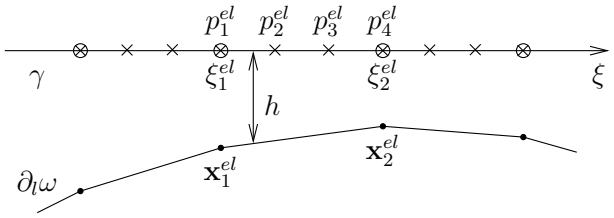


Fig. 2. Discretization of the lubricated boundary $\partial_l\omega$ into segments with linear interpolation of displacements ($m_h = 1$) and higher-order interpolation of lubricant pressure. The figure corresponds to $m_p = 3$ so that there are $m_p + 1 = 4$ pressure nodes per element.

The finite element formulation is obtained in a standard manner (e.g. Zienkiewicz and Taylor [14]). The finite element approximations of the unknown displacement and pressure fields are introduced, followed by element-wise numerical integration of the respective contributions. This leads to the set of nonlinear equations for unknown nodal displacements, pressures and Lagrange multipliers, the later enforcing the unilateral contact conditions. The only non-standard part in this procedure is the treatment of the Reynolds equation and this is commented in more detail below. The case of axial symmetry is only considered so that the solid part is analyzed in two-dimensions and the Reynolds equation is one-dimensional.

It is generally accepted that finite deformations, particularly in the case of nearly incompressible materials, are most efficiently resolved using low-order elements which, however, require special treatment of shear and volumetric locking effects using techniques such as enhanced assumed strain or mixed formulations, reduced integration, and others. In this work, an underintegrated axisymmetric four-node element is used which employs volumetric-deviatoric split and Taylor expansion of shape functions (Korelc [15]).

Importantly, the use of low-order solid elements implies that the boundary is discretized into line segments with piecewise-linear interpolation of displacements. The surface traction terms in the weak form (1) are evaluated along these segments. Consider thus the lubricated boundary $\partial_l\Omega$ discretized into finite elements, each formed by a line segment with two displacement nodes. In the deformed configuration, the position of a typical element, cf. Fig. 2, is specified by the current positions $\mathbf{x}_1^{el}$ and $\mathbf{x}_2^{el}$ of the two nodes. Projection of all the elements of the discretized deformed surface $\partial_l\omega$ onto the nominal contact surface $\gamma$ defines the discretization of the domain $\gamma$ into finite elements used to solve the Reynolds equation, cf. Fig. 2.

The Reynolds equation involves two fields, namely the pressure $p$ (the basic unknown) and the film thickness $h$. Linear interpolation of the displacements implies linear interpolation of the film thickness (first-order interpolation, $m_h = 1$). However, arbitrary interpolation order can be adopted for the pressure. Interpolation orders ranging from $m_p = 1$ (linear interpolation) to

$m_p = 5$ have been tested and it turns out that higher-order interpolations has a positive effect on the accuracy and stability of the method, with a relatively small overhead on the total number of unknowns and on the overall computational cost. Detailed results concerning convergence of the method with mesh refinement and pressure interpolation order will be reported elsewhere (selected results are provided in Section 4). Based on these studies interpolation order $m_p = 4$ has been chosen and used to study the dynamic sealing performance of O-ring and rectangular seals in Section 4.

The convergence studies revealed also spurious oscillations of pressure and film thickness which occur in severe lubrication conditions, typically at lower rod speeds and at higher sealed pressures. It has been observed that these oscillations are reduced by increasing the mesh density and, with a much weaker effect, by increasing the interpolation order of the pressure. Application of the discontinuous Galerkin method (which appears to be efficient in the case of the classical hard EHL line contact problems, cf. Lu et al. [16]) does not help significantly.

Computer implementation has been performed in the *AceGen/AceFEM* environment (Korelc [15,17]). The *AceGen* symbolic code generation system is used to automatically derive the characteristic expressions (e.g. element residual and tangent) and to generate the necessary numerical codes. The computations have been carried out in the *AceFEM* finite element environment.

### *3.2 Solution strategy*

The finite element discretization transforms the continuum problem defined in Section 2 to a set of nonlinear equations. These equations are solved monolithically for all global unknowns (displacements, pressures and Lagrange multipliers) using the iterative Newton method.

The exact tangent matrix, required in the Newton method, is obtained in a standard manner by linearization of the finite element equations. Here, all the dependencies related to the coupling of the solid and lubrication parts have to be taken into account. These include the dependence of the surface traction $\mathbf{t}$ on the lubricant pressure $p$ and its gradient, as well as the dependence of the film thickness $h$ on the displacements. Furthermore, the domain $\gamma$, on which the Reynolds equation is solved, and its discretization depend on the displacements. This dependence is also accounted for in the tangent matrix. Naturally, the global tangent matrix is not symmetric.

The Newton method converges to the solution only when the initial estimate (starting point of the iterative procedure) is sufficiently close to the solution. As the problem at hand is highly nonlinear (finite configuration changes, elas-

tohydrodynamic coupling, cavitation, etc.), a kind of path-following solution strategy has been developed, as outlined below.

In steady-state lubrication conditions, considered in this work, the solution depends on two process parameters, namely the sealed pressure $p_s$ and the rod speed $U$. The solution is obtained in the following steps. In the first step, the contact problem of the seal loaded by the hydrostatic pressure $p_s$ is solved incrementally by increasing the pressure from zero to $p_s$. At this stage, the lubricated contact is replaced by the frictionless contact between the seal and the rod. In the second step, the seal-rod contact is gradually switched from the simple frictionless contact to the hydrodynamic lubrication. At this stage, a high rod speed is assumed, for which the EHL problem is solved more easily. Finally, in the third step, the rod speed is gradually decreased to the desired value.

In a typical situation, it is of interest to find the solution for a range of pressures and rod velocities. One of the advantages of the above procedure is that the third step directly provides the response for a range of rod velocities at a fixed sealed pressure.

The solution strategy described above proved to be efficient in the majority of cases analyzed in this work. Additional treatment was necessary only in the most demanding cases. In such cases, an intermediate solution was found by neglecting the shear stresses on the lubricated boundary, i.e. by putting $\tau = 0$ in Eq. (17), and subsequently the shear stresses were increased to the actual value. In a very few cases, a converged solution could not be achieved, see Section 4.2.

## 4 Numerical examples

### *4.1 O-ring seal*

The dynamic sealing performance of an O-ring seal in steady-state lubrication conditions has been studied as the first example. The basic geometrical, material and process parameters used in the computations are provided in Table 1. The elastic properties [3] of the seal correspond to the NBR rubber (70 ShA hardness) while the viscosity is that of the Shell Tellus 46 oil at the working temperature of 30°C.

[3] Estimated values of parameters $\mu_1$ and $\mu_2$. Bulk modulus $\kappa$ is adopted arbitrarily (sufficiently high to ensure nearly incompressible behaviour with the restriction imposed by the performance of the displacement-based solid elements used in the present study).

Table 1
O-ring seal: geometrical, material and process parameters.

| | | | |
|---|---|---|---|
| Inner diameter of the seal | $D_{\text{inner}}$ | 50.39 | mm |
| Diameter of the seal (cross-section) | $D_{\text{seal}}$ | 3.53 | mm |
| Rod diameter | $D_{\text{rod}}$ | 50.00 | mm |
| Inner diameter of the housing | $D_{\text{hous}}$ | 56.30 | mm |
| Elastic parameters of the seal | $\mu_1$ | 3.04 | MPa |
| | $\mu_2$ | 0.62 | MPa |
| | $\kappa$ | 500 | MPa |
| Oil viscosity (HLP 46) at 30°C | $\eta_0$ | $6.59 \times 10^{-8}$ | MPa s |
| Pressure-viscosity coefficient | $\alpha$ | 0.02 | 1/MPa |
| Cavitation penalty parameter | $\epsilon$ | $10^4$ | mm/(MPa s) |
| Rod speed | $U$ | ±25–1600 | mm/s |
| Sealed pressure | $p_s$ | 0–5 | MPa |

Table 2
O-ring seal: number of elements and unknowns of the finite element mesh.

| | No. of solid elements | No. of segments for Reynolds eq. | Total No. of unknowns ($m_p = 4$) | No. of pressure unknowns ($m_p = 4$) |
|---|---|---|---|---|
| mesh density 1 | 420 | 27 | 1076 | 109 |
| mesh density 2 | 1560 | 54 | 3587 | 217 |
| mesh density 4 | 6000 | 108 | 12929 | 433 |
| mesh density 8 | 23520 | 216 | 48893 | 865 |
| mesh density 16 | 93120 | 432 | 189941 | 1729 |

A structured finite element mesh, significantly refined along the lubricated boundary, has been developed. Five mesh densities have been used in the computations, cf. Table 2, so that convergence with mesh refinement could be examined. Figure 3 shows the undeformed meshes corresponding to the three coarser mesh densities (1, 2 and 4). The deformed configurations corresponding to the sealed pressure $p_s$ equal to 0, 1 and 5 MPa are shown in Fig. 4.

As already discussed in Section 3, the solution may exhibit oscillations of pressure and film thickness if the mesh is not fine enough. Generally, the lower the rod speed and the higher the sealed pressure, the finer mesh is necessary to prevent the oscillations. At the same time, moderate oscillations (occurring typically in the vicinity of the sudden drop of the film thickness in the outlet zone) do not significantly affect the overall solution nor leakage predictions.

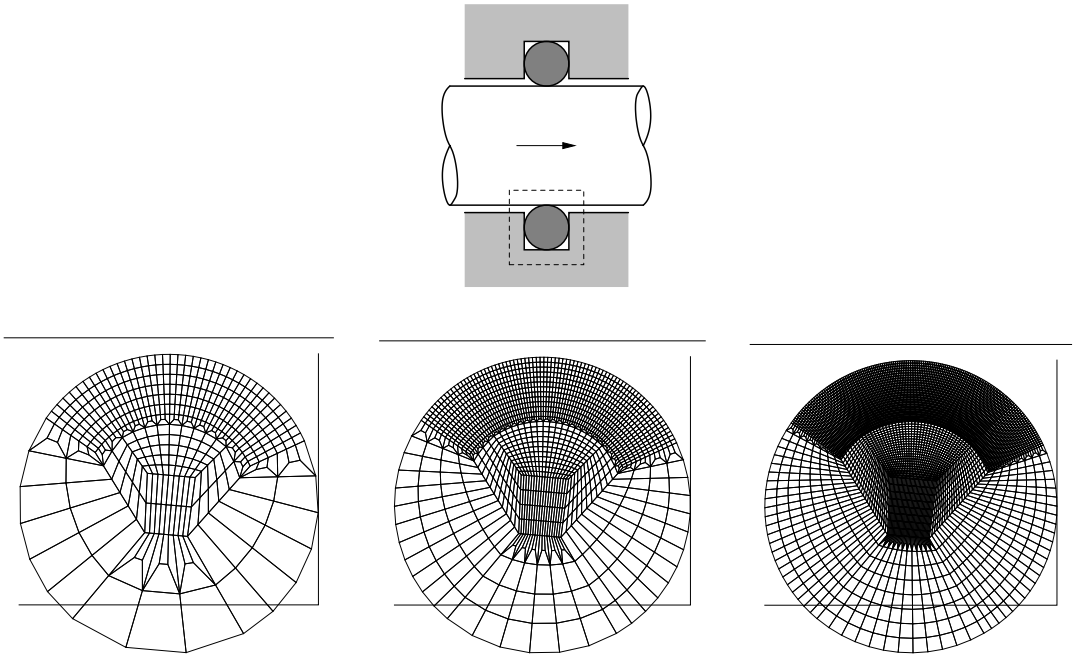

(a) (b) (c)

Fig. 3. O-ring seal in undeformed configuration: finite element mesh for (a) mesh density 1, (b) mesh density 2 and (c) mesh density 4. The contact surfaces of the rod and housing are indicated by solid lines. The rod is on the top and the sealed-pressure side is on the left.

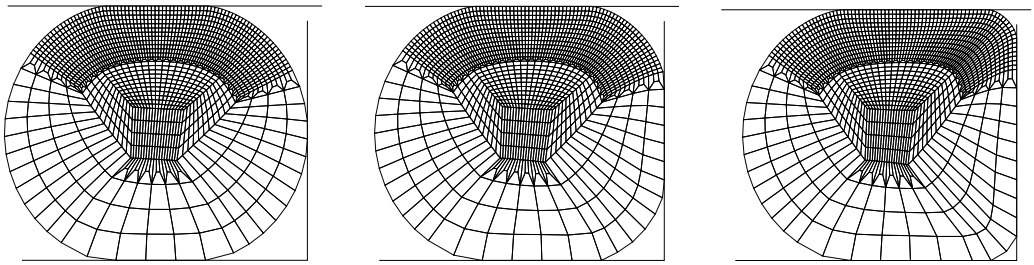

(a) (b) (c)

Fig. 4. O-ring seal in deformed configuration: finite element mesh (mesh density 2) for sealed pressure (a) $p_s = 0$, (b) $p_s = 1\,\mathrm{MPa}$ and (c) $p_s = 5\,\mathrm{MPa}$. The contact surfaces of the rod and housing are indicated by solid lines.

For instance, for $p_s = 1\,\mathrm{MPa}$ and $U = 400\,\mathrm{mm/s}$, the leakage rate predicted for mesh density 4 is less than 0.1% lower than the converged value obtained for mesh density 16, except for $m_p = 1$ where the corresponding error is 2%. This is illustrated in Fig. 5 which shows the convergence of the leakage rate with mesh refinement and pressure interpolation order. Here and below, the leakage rate is represented by the parameter $h^*$,

$$h^* = \frac{q}{\bar{u}} = \frac{2q}{U}, \tag{19}$$

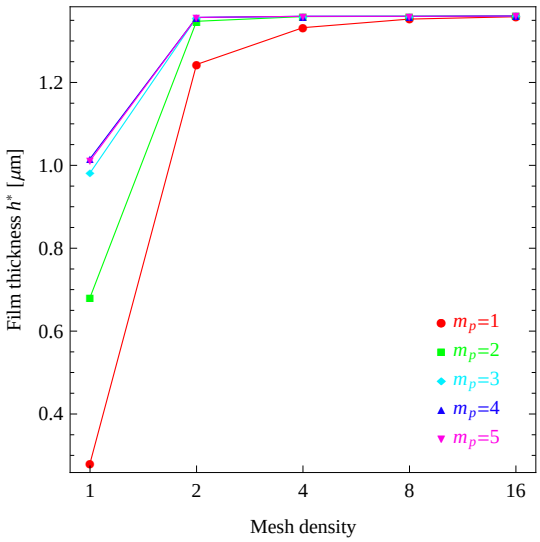


Fig. 5. O-ring seal: convergence of the leakage rate represented by $h^* = q/\bar{u}$ with mesh refinement (outstroke, $p_s = 1\,\mathrm{MPa}$, $U = 400\,\mathrm{mm/s}$).

which can also be interpreted as the film thickness at the point of maximum pressure (where $\mathrm{d}p/\mathrm{d}\xi = 0$), cf. Eq. $(11)_2$.

All the detailed results reported below correspond to mesh density 16. This mesh provides reliable results in the whole range of lubrication conditions specified in Table 1, although small oscillations are observed in the most severe conditions, as it is seen, for instance, in Figs. 6(d) and 7(d) below. Note that highly accurate results are obtained also for mesh density 8 except in the case of instroke at the severest lubrication conditions in which film thickness drops below $h = 0.2\,\mu\mathrm{m}$.

Figures 6 and 7 present sample detailed results obtained for the O-ring seal. Pressure profile and lubricant film thickness are shown for the rod speed $U = 100\,\mathrm{mm/s}$ and for selected values of the sealed pressure $p_s$ during outstroke and instroke, and the respective quantities corresponding to $p_s = 3\,\mathrm{MPa}$ are compared in Fig. 7, including the details of the inlet and outlet zones shown in Fig. 7(c,d). Here, the position $\xi = 0$ corresponds to the center of the cross section of the seal in the undeformed configuration, cf. Fig. 3. Although the friction forces change direction when the direction of motion is reversed, the action of the sealed pressure prevents the seal from moving in its housing and thus the pressure distributions for outstroke and instroke are remarkably close, cf. Fig. 7(a,c).

The overall dynamic sealing performance is conveniently characterized by the parameter $h^* = q/\bar{u}$. Figures 8 and 9 show the effect of the sealed pressure $p_s$ and the rod speed $U$ on the leakage rate represented by $h^*$.

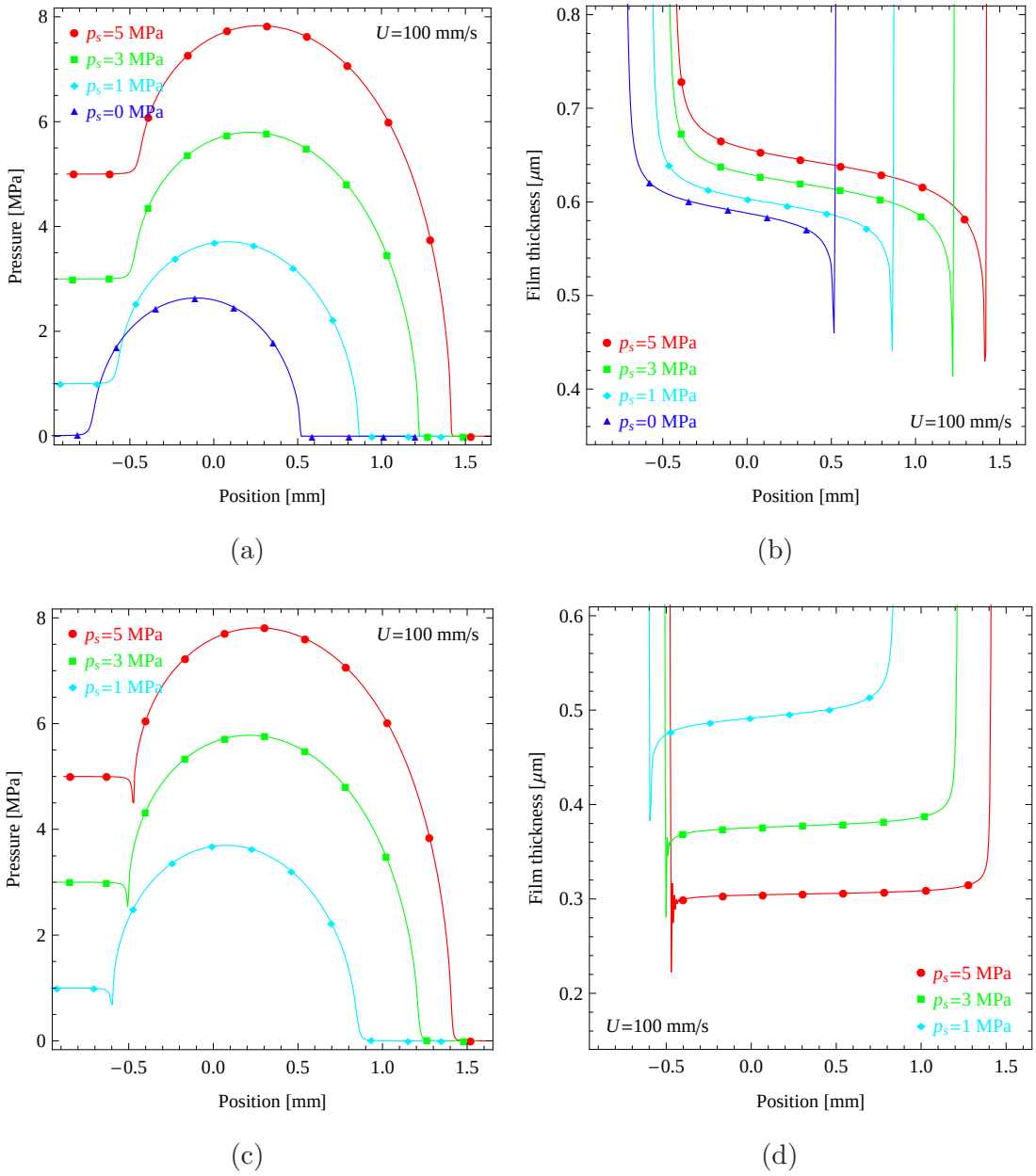


Fig. 6. O-ring seal: pressure profile (a,c) and film thickness (b,d) during outstroke (a,b) and instroke (c,d) at the rod speed $U = 100\,\mathrm{mm/s}$.

### *4.2 Rectangular seal*

Elastomeric seal of rectangular cross-section is studied as the second example. The basic geometrical, material and process parameters used in the computations are provided in Table 3. The geometrical parameters correspond to those used by Nikas [9,10] (the outer diameter of the seal is not specified in [9,10] thus the value of $D_{\mathrm{outer}} = 60.2\,\mathrm{mm}$ has been chosen arbitrarily). In order to study the effect of corner radius $R$, the values $R = 0.1\,\mathrm{mm}$ and $R = 0.4\,\mathrm{mm}$ have been studied in addition to $R = 0.2\,\mathrm{mm}$, as specified by Nikas [9,10].

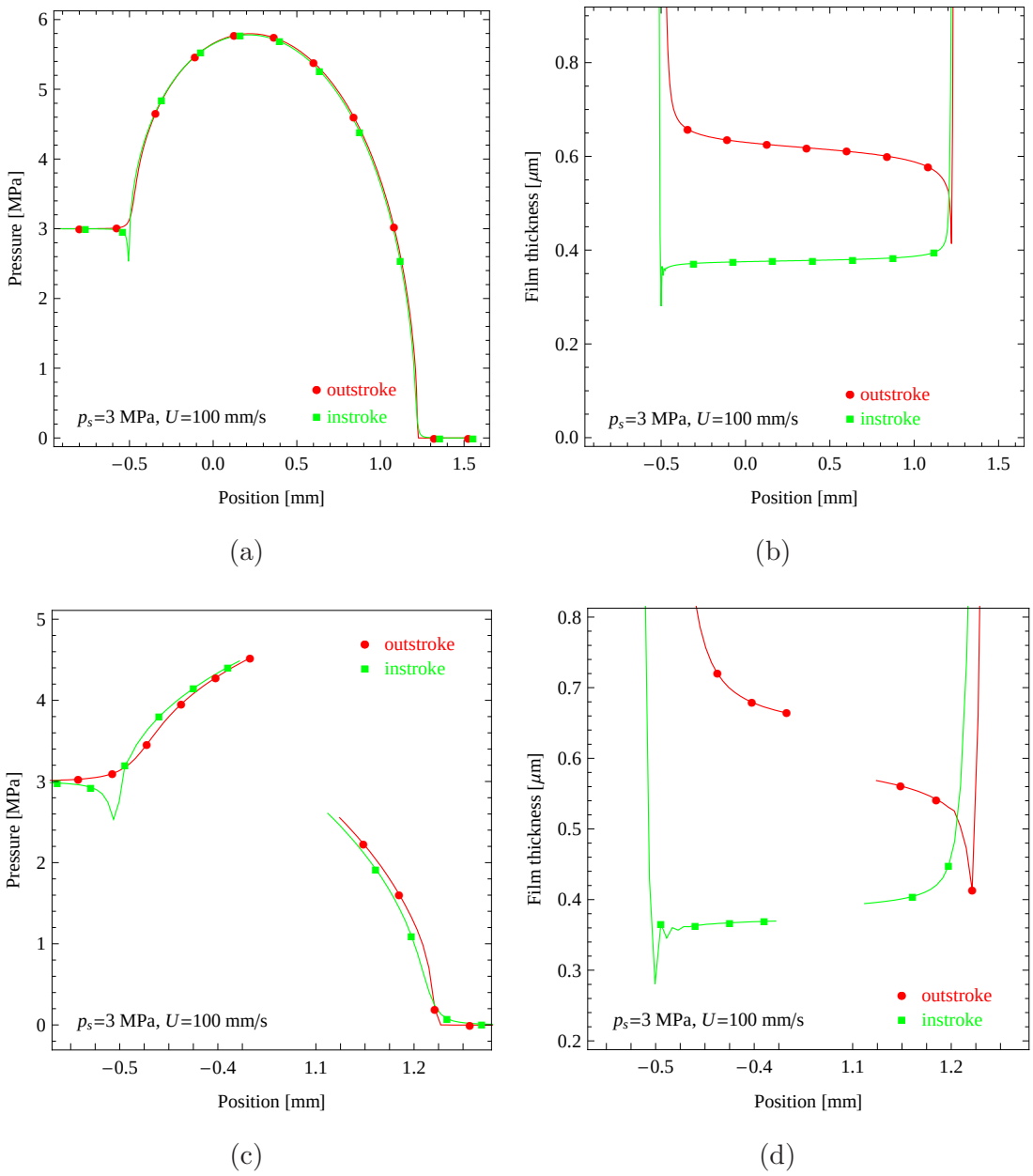


Fig. 7. O-ring seal: pressure profile (a,c) and film thickness (b,d) during outstroke and instroke for the sealed pressure $p_s = 3\,\mathrm{MPa}$ and the rod speed $U = 100\,\mathrm{mm/s}$.

Elastic properties of the elastomeric seal and oil viscosity are those used in the O-ring example above.

Again, a family of structured finite element meshes has been developed which is shown in Fig. 10. The mesh is significantly refined in the vicinity of the lubricated contact surface and in particular in the vicinity of corners. Rounding of the outer corners has been neglected as it has a negligible effect on the contact stresses at the lubricated surface. A very coarse mesh can thus be used in that region so that the total number of unknowns is reduced. Table 4 provides the number of elements and unknowns for five mesh densities used in the present

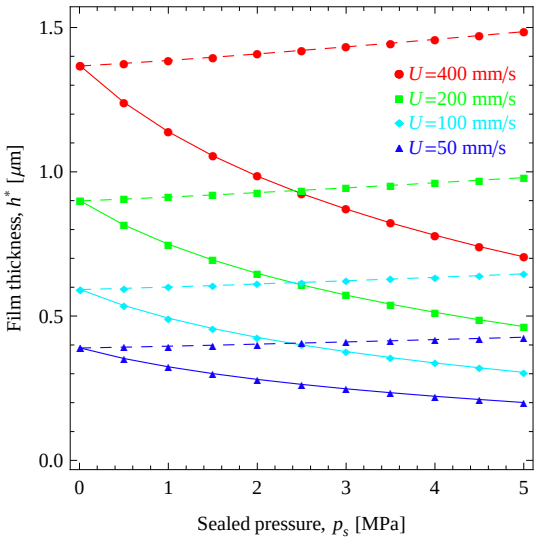


Fig. 8. O-ring seal: parameter $h^* = q/\bar{u}$ as a function of the sealed pressure $p_s$ (instroke – solid lines, outstroke – dashed lines).

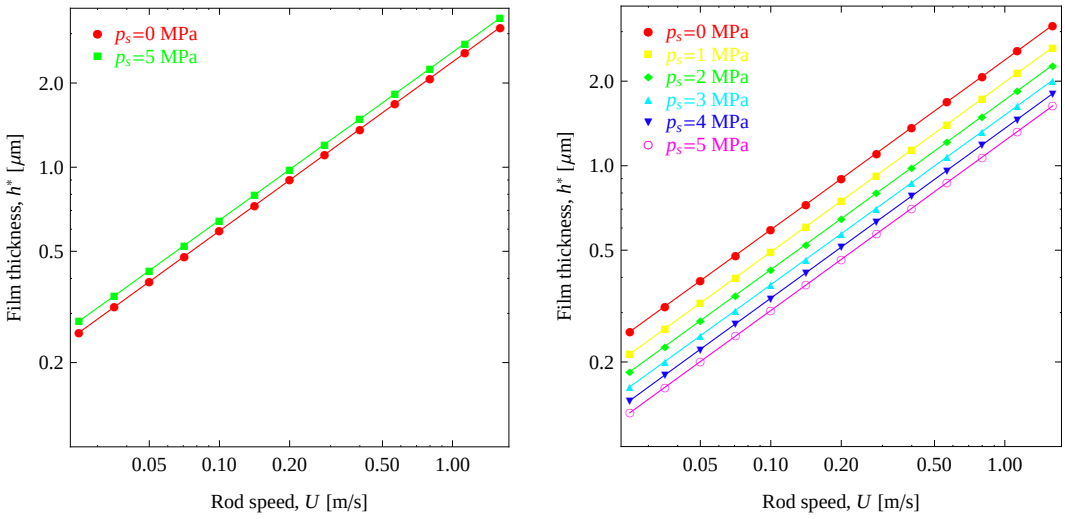


(a) (b)

Fig. 9. O-ring seal: parameter $h^* = q/\bar{u}$ as a function of the rod speed $U$ for (a) outstroke and (b) instroke (log-log plots).

study. Results obtained for the finest mesh density 16 are reported below, although convergence studies revealed that in less severe lubrication conditions (i.e. at lower sealed pressures and/or at higher rod speeds) coarser meshes provide satisfactory results. Position $\xi = 0$ in the figures below corresponds to the sealed-pressure side face of the seal in the undeformed configuration.

Upon application of the sealed pressure, it is the air-side corner that deforms most and the configuration changes in this zone are significant, cf. Fig. 11. The deformation pattern and, in general, the qualitative features of the solution

Table 3
Rectangular seal: geometrical, material and process parameters.

| | | | |
|---|---|---|---|
| Inner diameter of the seal | $D_{\text{inner}}$ | 49.9 | mm |
| Outer diameter of the seal | $D_{\text{outer}}$ | 60.2 | mm |
| Seal width | $w$ | 3.5 | mm |
| Corner radius | $R$ | 0.1, 0.2, 0.4 | mm |
| Rod diameter | $D_{\text{rod}}$ | 50.0 | mm |
| Inner diameter of the housing | $D_{\text{hous}}$ | 60.0 | mm |
| Elastic parameters of the seal | $\mu_1$ | 3.04 | MPa |
| | $\mu_2$ | 0.62 | MPa |
| | $\kappa$ | 500 | MPa |
| Oil viscosity (HLP 46) at 30°C | $\eta_0$ | $6.59 \times 10^{-8}$ | MPa s |
| Pressure-viscosity coefficient | $\alpha$ | 0.02 | 1/MPa |
| Cavitation penalty parameter | $\epsilon$ | $10^4$ | mm/(MPa s) |
| Rod speed | $U$ | ±25–1600 | mm/s |
| Sealed pressure | $p_s$ | 0–10 | MPa |

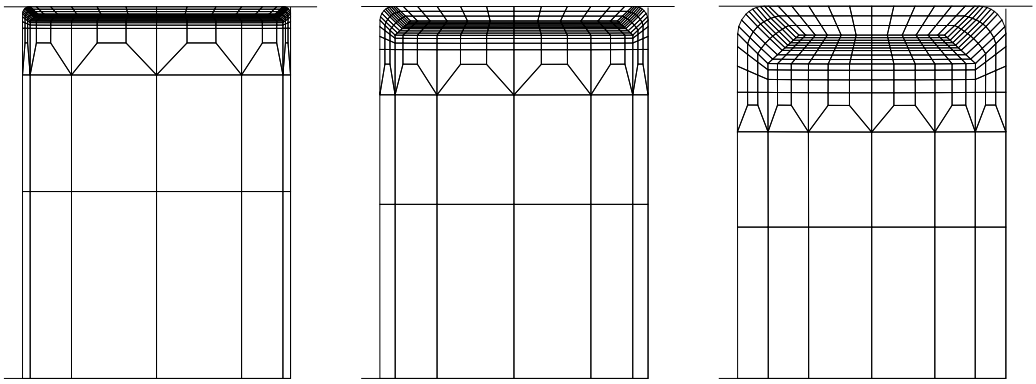

(a) $R = 0.1\,\text{mm}$ (b) $R = 0.2\,\text{mm}$ (c) $R = 0.4\,\text{mm}$

Fig. 10. Rectangular seal: finite element mesh (mesh density 1) in the deformed configuration corresponding to zero sealed pressure ($p_s = 0$) and corner radius (a) $R = 0.1\,\text{mm}$, (b) $R = 0.2\,\text{mm}$ and (c) $R = 0.4\,\text{mm}$.

are essentially independent of the corner radius. This is visible, for instance, on the diagrams of pressure which exhibit two peaks at the corners and a plateau between them, cf. Fig. 12(a,c). Note that similar pressure peaks at the rounded corners have been measured and also predicted by Prati and Strozzi [6]. In the case of instroke, the pressure profiles are additionally characterized by a pressure drop in the outlet zone, cf. Fig. 12(c). Similar effect is excluded in the case of outstroke due to the cavitation condition $p \geq 0$.

Table 4
Rectangular seal: number of elements and unknowns of the finite element mesh.

| | No. of solid elements | No. of segments for Reynolds eq. | Total No. of unknowns ($m_p = 4$) | No. of pressure unknowns ($m_p = 4$) |
|---|---|---|---|---|
| mesh density 1 | 288 | 24 | 735 | 97 |
| mesh density 2 | 1116 | 48 | 2550 | 193 |
| mesh density 4 | 4392 | 96 | 9420 | 385 |
| mesh density 8 | 17424 | 192 | 36120 | 769 |
| mesh density 16 | 69408 | 384 | 141360 | 1537 |

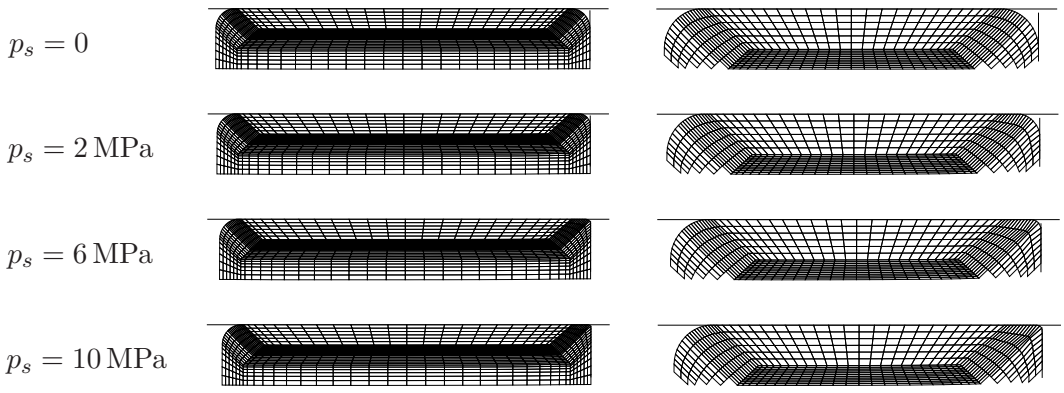


(a) $R = 0.2\,\mathrm{mm}$ (b) $R = 0.4\,\mathrm{mm}$

Fig. 11. Rectangular seal: details of the deformed finite element mesh (mesh density 2) corresponding to different values of the sealed pressure $p_s$ and corner radius (a) $R = 0.2\,\mathrm{mm}$ and (b) $R = 0.4\,\mathrm{mm}$.

The significant effect of the corner radius on the thickness of the lubricant film is clearly visible in Fig. 12(b,d), however, the qualitative features are not affected. Both in the case of the outstroke and the instroke, the film thickness exhibits a local minimum in the inlet zone, followed by a plateau and, in the outlet zone, a local maximum next to a global minimum. These features, shown in more detail in Fig. 13, are observed in the whole range of process parameters analyzed in this work and thus seem to be characteristic for the EHL problem at hand.

The effect of the sealed pressure $p_s$ on pressure profile and film thickness is illustrated in Fig. 14 for the case of corner radius $R = 0.4\,\mathrm{mm}$ for which the details of the inlet and outlet zones are better visible (while the general pattern is fully representative for the other cases, as discussed above).

Figures 15 and 16 present the leakage rate, represented by parameter $h^* = q/\bar{u}$, as a function of the rod speed and pressure, respectively. Qualitatively, the results are similar to those obtained for the O-ring seal in Section 4.1. The

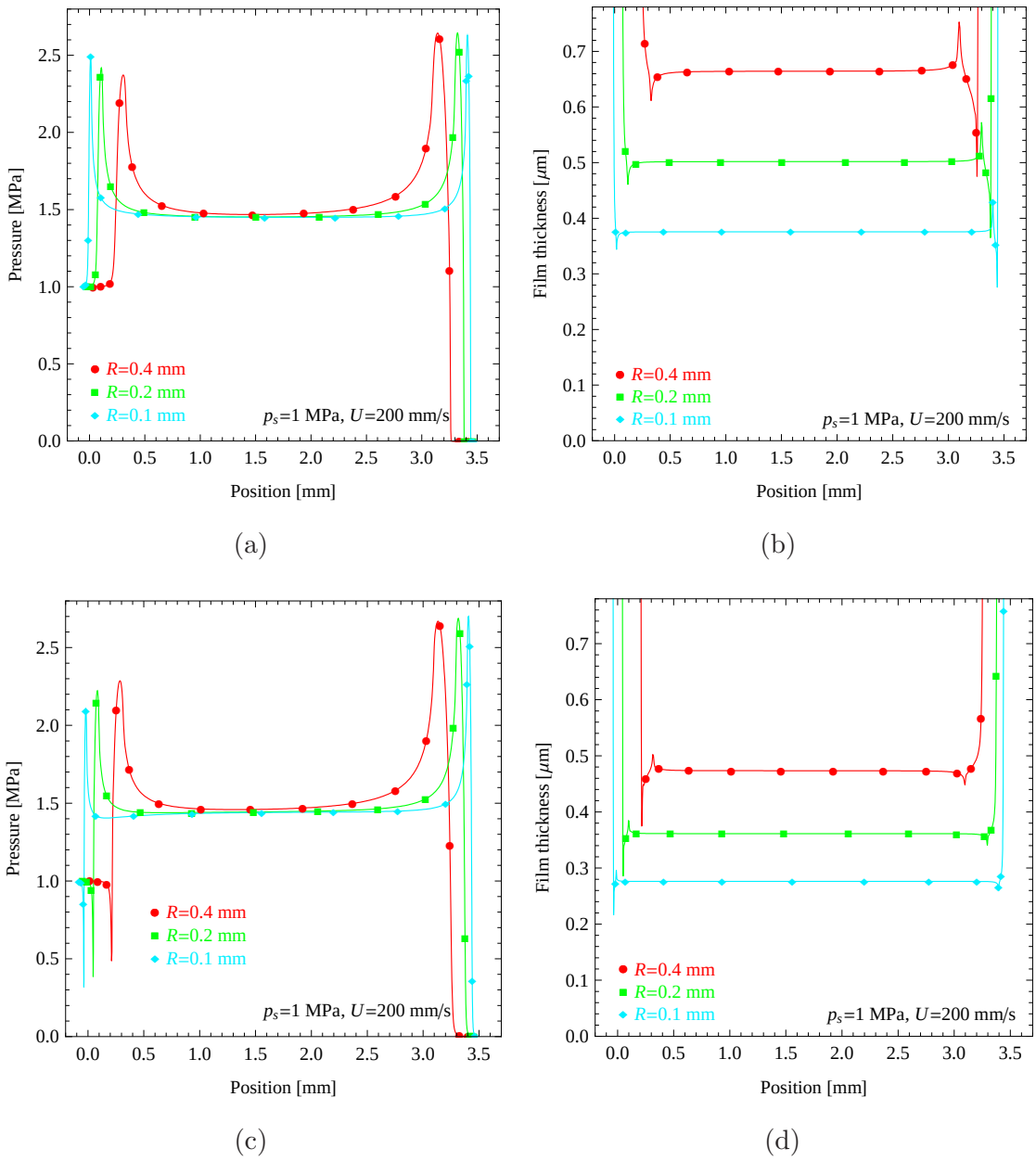


Fig. 12. Rectangular seal: pressure profile (a,c) and film thickness (b,d) during steady-state outstroke (a,b) and instroke (c,d) for the sealed pressure $p_s = 1\,\mathrm{MPa}$ and the rod speed $U = 200\,\mathrm{mm/s}$.

essential effect of the corner radius on the leakage rate is illustrated in Fig. 17. As mentioned in Section 3.2, in some cases the adopted solution strategy failed to provide converged results, hence the missing data points in Figs. 15–17.

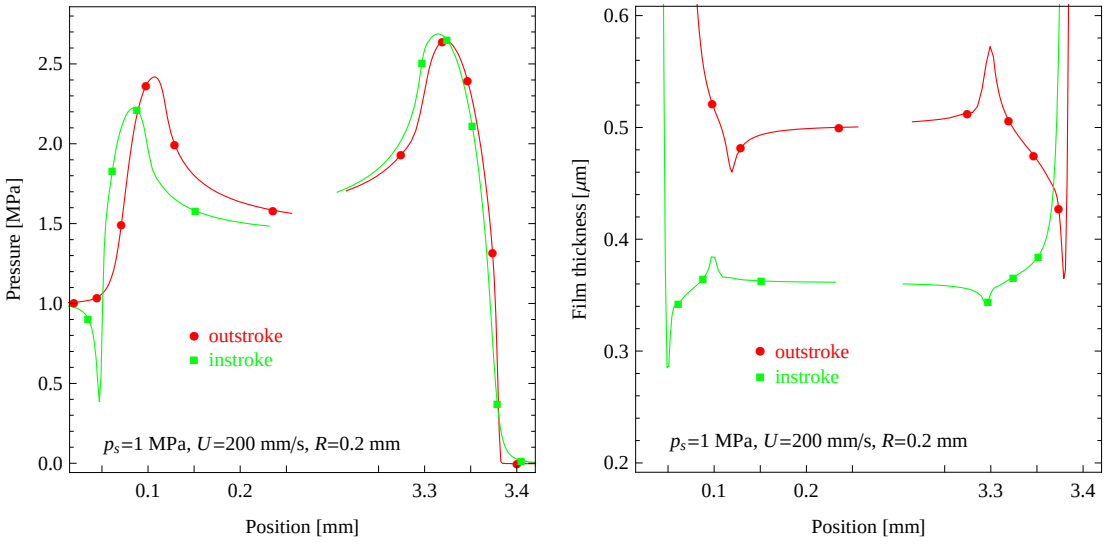


(a) (b)

Fig. 13. Rectangular seal: details of pressure profile (a) and film thickness (b) during outstroke and instroke for the sealed pressure $p_s = 1\,\mathrm{MPa}$ and the rod speed $U = 200\,\mathrm{mm/s}$.

### *4.3 Effect of friction*

All the results presented in the preceding subsections have been obtained with full account of friction due to the shear stresses in the lubricant film. Note that it is commonly assumed in the EHL theory, both for hard and soft EHL problems, that these stresses can be neglected in the analysis of deformations of the contacting bodies. Accordingly, additional computations have been carried out in order to verify the validity of this assumption.

Considering the leading first term in Eq. (18), the magnitude of the shear stress $\tau$ can be estimated to be of the order of 0.01–0.1 MPa in the range of process parameters covered by the present study. These values are 2–3 orders of magnitude smaller than the hydrodynamic pressures and the shear modulus of the elastomeric seal.

The EHL simulations of the O-ring seal and the rectangular seal have thus been repeated with friction neglected, i.e. by assuming that the shear stress $\tau$ in Eq. 17 vanishes. Firstly, it has been observed that the EHL problems with no friction converge more easily than the corresponding problems with friction. In particular, convergence problems were encountered only in the case of rectangular seal with the corner radius $R = 0.1\,\mathrm{mm}$ and sealed pressure $p_s = 9$–$10\,\mathrm{MPa}$.

As the predictions of the dynamic sealing performance are considered, the effect on the leakage rate appears to be negligible in the case of the O-ring seal –

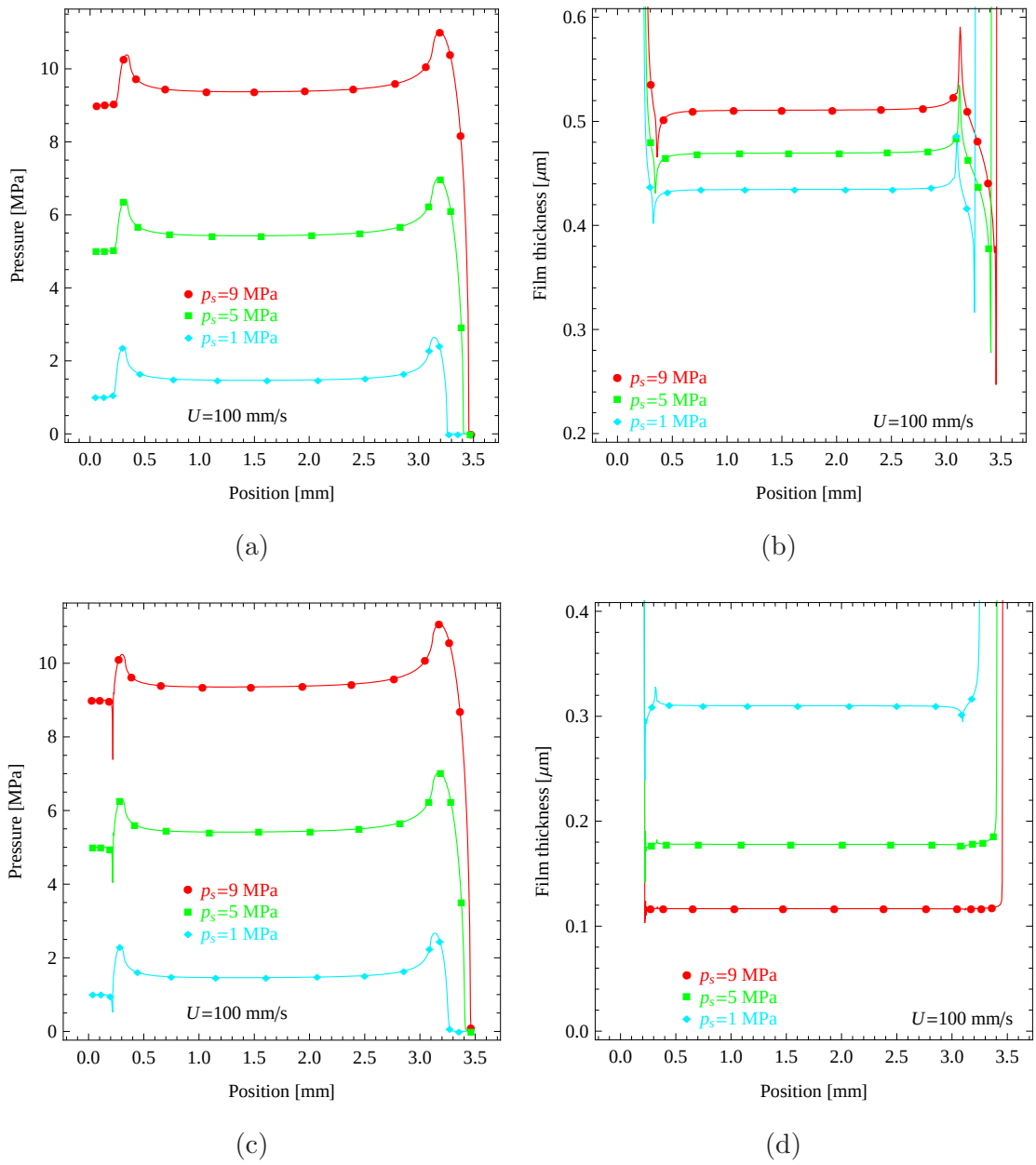


Fig. 14. Rectangular seal: pressure profile (a,c) and film thickness (b,d) during outstroke (a,b) and instroke (c,d) for the rod speed $U = 100\,\mathrm{mm/s}$ and the corner radius $R = 0.4\,\mathrm{mm}$.

the error introduced by neglecting friction stresses is at most 1% in the range of sealed pressures and rod speeds covered by the present study. However, in the case of the rectangular seal, the corresponding error reaches 10–15%. This is illustrated in Fig. 18 which presents the leakage rate represented by parameter $h^*_{\mathrm{no\,friction}}$, corresponding to the simplified case with friction neglected, normalized by the leakage rate $h^*_{\mathrm{friction}}$ obtained from the full analysis. The error is higher for the outstroke than for the instroke and increases with increasing rod speed and with decreasing corner radius. The latter effect is expected in view of the results presented in the previous section – the film thickness decreases

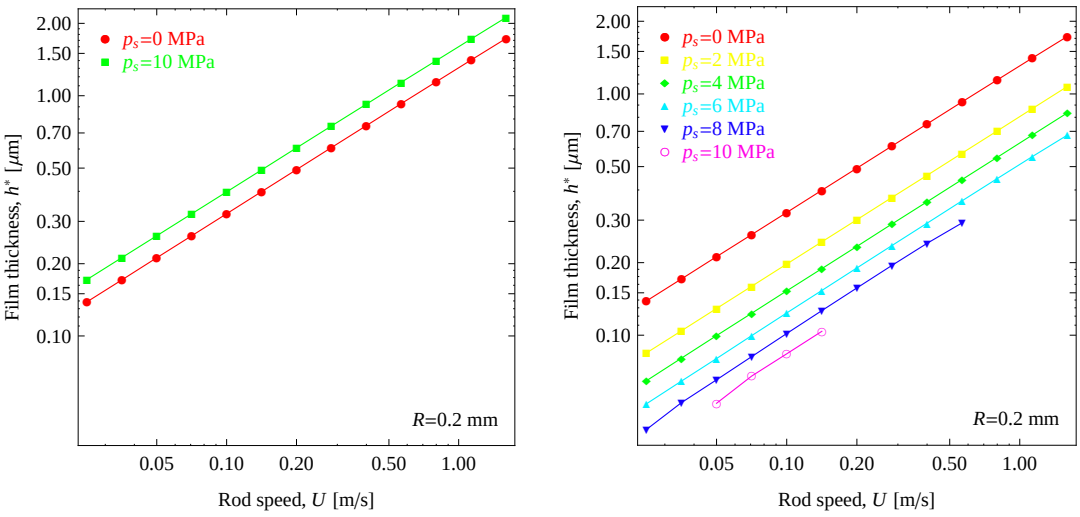


(a) (b)

Fig. 15. Rectangular seal: parameter $h^* = q/\bar{u}$ as a function of the rod speed $U$ for (a) outstroke and (b) instroke (corner radius $R = 0.2\,\mathrm{mm}$).

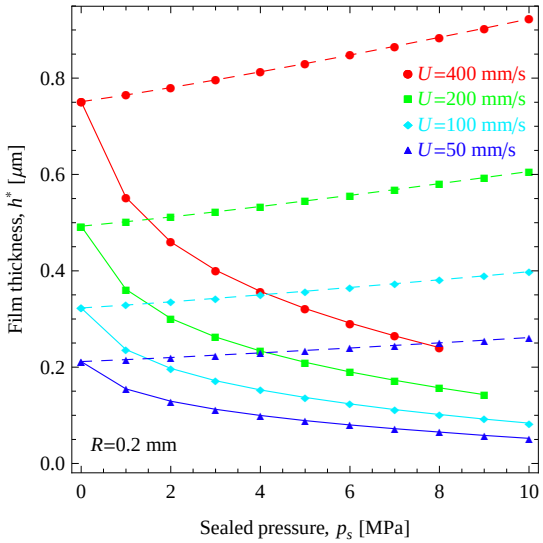


Fig. 16. Rectangular seal: parameter $h^* = q/\bar{u}$ as a function of the sealed pressure $p_s$ for the corner radius $R = 0.2\,\mathrm{mm}$ (instroke – solid lines, outstroke – dashed lines).

with decreasing corner radius, and thus the shear stresses in the lubricant film increase at a fixed rod speed.

Clearly, the effect of friction on the overall leakage rate is associated with a variation of the local quantities. These local effects are illustrated in Fig. 19. At the high rod speed $U = 800\,\mathrm{mm/s}$, the effect of friction is significant, particularly, at the sealed-pressure side. During the outstroke, the friction stresses induce compressive in-plane stresses along the contact interface and the pressure at the sealed-pressure side increases with respect to the frictionless

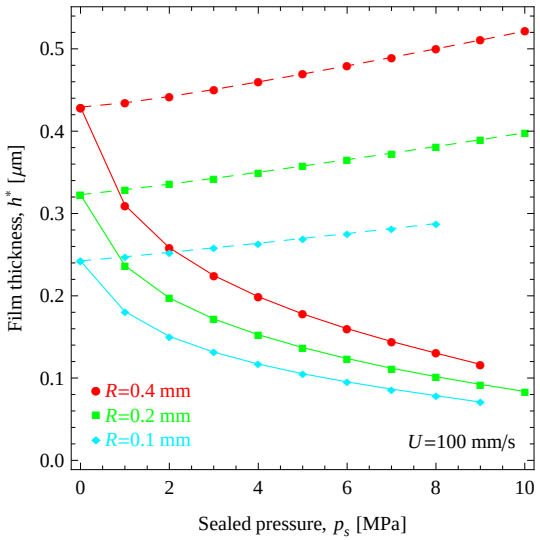


Fig. 17. Rectangular seal: parameter $h^* = q/\bar{u}$ as a function of the sealed pressure $p_s$ and the corner radius $R$ (instroke – solid lines, outstroke – dashed lines).

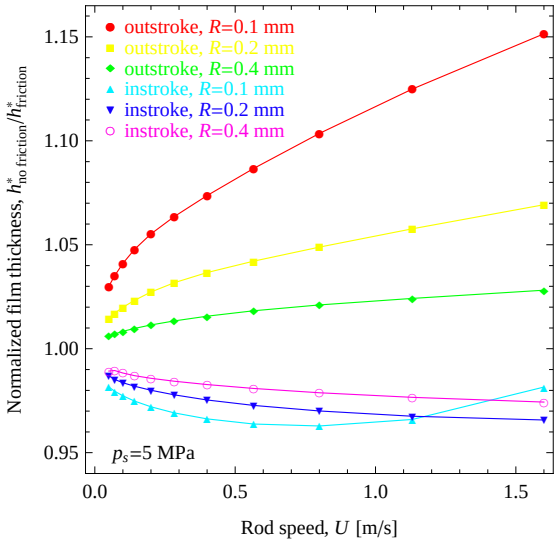


Fig. 18. Effect of friction on the leakage rate in the rectangular seal: parameter $h^*_{\text{no friction}}$ normalized by $h^*_{\text{friction}}$ (see text).

case. An opposite effect is observed during the instroke.

## 5 Conclusion and discussion

A solution method for the soft EHL problems of reciprocating elastomeric seals has been developed. The formulation takes full account of the finite deformations of the seal and of the coupling of the solid and fluid parts, including friction due to shear stresses in the lubricant film. The corresponding computational framework employs the finite element method to solve the equilibrium

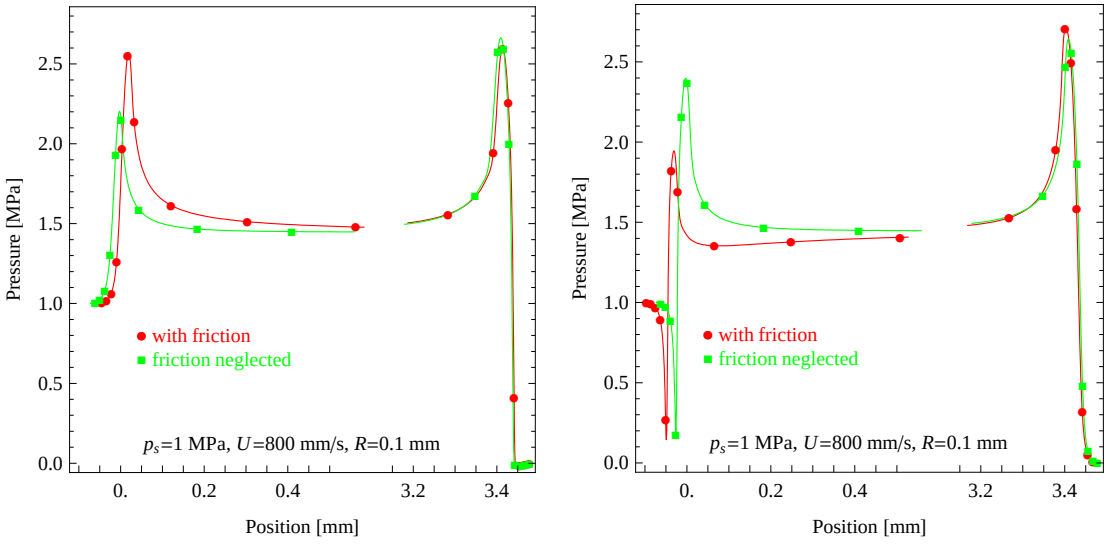


Fig. 19. Rectangular seal: effect of friction on the pressure in the inlet and outlet zones for (a) outstroke and (b) instroke.

equation for the seal as well as the Reynolds equation describing the flow of the lubricant. The resulting nonlinear equations are solved using the Newton method, however, a special solution strategy (a kind of a path-following method) had to be employed in order to ensure the convergence of the Newton method. The approach has been applied to study the steady-state hydrodynamic lubrication in reciprocating O-ring and rectangular seals and detailed results obtained for these benchmark problems have been reported. Specifically, the characteristic features of the solutions have been illustrated as well as the predictions concerning the dynamic sealing performance of the seals. Furthermore, it has been shown that the effects of friction stresses may be significant and thus cannot be neglected *a priori*. To the best of the authors' knowledge, a formulation consistently treating finite configuration changes with a corresponding computational scheme have not been reported in the literature so far.

The finite configuration changes are clearly visible in the case of the O-ring seal, as the whole cross-section significantly deforms upon loading by the sealed pressure. This issue is less obvious in the case of the rectangular seal, however, the related effects are essential also in that case. In fact, the air-side corner deforms severely and, although it constitutes only a small fraction of the cross-section, this significantly affects the geometry of the inlet zone at instroke and of the outlet zone at outstroke.

In view of the geometrical and material nonlinearities, solution of the deformation problem for the seal is only possible using the finite element method (or another computational technique) and requires discretization of the whole

cross-section. Consequently, the degrees of freedom directly involved in the Reynolds equation (nodal pressures and nodal displacements at the contact surface) constitute only a small fraction of the global unknowns, and this ratio decreases with mesh refinement. For instance, the finest meshes, which were necessary for the analysis of the most demanding cases, involved more than one hundred thousand unknowns, of which the pressure unknowns were only about one per cent.

In the numerical examples, attention has been paid to the issues of accuracy and convergence of the solutions with mesh refinement. Discussion of the related effects and selected results have been presented in this paper, however, the detailed results of the convergence studies will be presented in a separate contribution. It has been observed that the severer the lubrication conditions the finer mesh is necessary to obtain an accurate and oscillation-free solution (severe lubrication conditions occur at low rod speeds and at high sealed pressures, furthermore, the instroke is usually more demanding than the outstroke). In fact, if the mesh is not sufficiently fine, then spurious oscillations of pressure and film thickness occur, which may additionally lead to convergence problems. At the same time, mild oscillations do not significantly affect the overall solution, including the leakage rate.

Obviously, refinement of the finite element mesh results in the increase of the computational cost. However, this cost is not prohibitive even for the finest meshes used in the present study. For instance, in the case of the rectangular seal, the complete analysis of one loading case with the highest mesh density 16 takes 45 to 75 minutes on a 3.4 GHz Pentium 4 PC, of which 60–70 per cent are spent on the pure contact analysis of the seal loaded by the hydrostatic pressure (first stage of the procedure described in Section 3.2). Note that such a complete analysis provides the results for the whole range of rod speeds at a fixed sealed pressure. The corresponding CPU time drops down to 5–7 minutes for mesh density 8 and is less than one minute in the case of mesh density 4. The computational efficiency could probably be improved by using more optimal unstructured meshes and, in particular, by applying adaptive mesh refinement techniques.

Despite the numerical problems and restrictions mentioned above, the present approach is capable of providing solutions in a wide range of process parameters. Note that, at the lowest rod speed analyzed ($U = 25\,\mathrm{mm/s}$), the thickness of the lubricant film is as low as 0.1–0.2 $\mu$m in the case of the O-ring seal and 0.03–0.15 $\mu$m in the case of the rectangular seal. In these conditions, the effect of surface roughness is expected to be significant, in particular, the assumption of full-film hydrodynamic lubrication may be inadequate. The present results correspond to an idealized EHL problem for smooth surfaces. In order to include the effect of roughness, the flow-factor approach (cf. Patir and Cheng [18], Salant et al. [7]) seems more feasible than the direct treatment

of rough surfaces (e.g. Nikas [9]) in view of the required fine discretizations. On the other hand, the assumption of separation of scales may be inadequate in the zones of very high gradients of pressure and film thickness which have been revealed by the present analysis.

## Acknowledgement

This work has been financially supported by the European Commission through the PROHIPP project (NMP 2–CT–2004–505466).

## References

[1] B. Nau, An historical review of studies of polymeric seals in reciprocating hydraulic systems, Proc. Instn. Mech. Engrs. Part J: J. Engng. Tribol. 213 (1999) 215–226.

[2] D. Dowson, G. Higginson, Elasto-hydrodynamic Lubrication, Pergamon Press, 1977.

[3] H. Müller, B. Nau, Fluid Sealing Technology, Principles and Applications, Marcel Dekker, Inc., 1998.

[4] L. Ruskell, A rapidly converging theoretical solution of the elastohydrodynamic problem for rectangular rubber seals, Proc. Instn. Mech. Engrs. Part C: J. Mech. Engng. Sci. 22 (1980) 9–16.

[5] Y. Yang, W. Hughes, An elastohydrodynamic analysis of preloaded sliding seals, ASLE Trans. 27 (1983) 197–202.

[6] E. Prati, A. Strozzi, A study of the elastohydrodynamic problem in rectangular elastomeric seals, Trans. ASME J. Tribol. 106 (1984) 505–512.

[7] R. Salant, N. Maser, B. Yang, Numerical model of a reciprocating hydraulic rod seal, Trans. ASME J. Tribol. 129 (2007) 91–97.

[8] G. Field, B. Nau, A theoretical study of the elastohydrodynamic lubrication of reciprocating rubber seals, ASLE Trans. 18 (1974) 48–54.

[9] G. Nikas, Elastohydrodynamics and mechanics of rectangular elastomeric seals for reciprocating piston rods, Trans. ASME J. Tribol. 125 (2003) 60–69.

[10] G. Nikas, R. Sayles, Nonlinear elasticity of rectangular elastomeric seals and its effect on elastohydrodynamic numerical analysis, Tribol. Int. 37 (2004) 651–660.

[11] P. Wriggers, Computational Contact Mechanics, Wiley, Chichester, 2002.

[12] P. Alart, A. Curnier, A mixed formulation for frictional contact problems prone to Newton like solution methods, Comp. Meth. Appl. Mech. Engng. 92 (1991) 353–375.

[13] S. Wu, A penalty formulation and numerical approximation of the reynolds-hertz problem of elastohydrodynamic lubrication, Int. J. Engng. Sci. 24 (1986) 1001–1013.

[14] O. Zienkiewicz, R. Taylor, The Finite Element Method, 5th Edition, Butterworth-Heinemann, Oxford, 2000.

[15] J. Korelc, AceGen and AceFEM user manuals, Available at http://www.fgg.uni-lj.si/Symech/ (2006).

[16] H. Lu, M. Berzins, C. Goodyer, P. Jimack, High-order discontinuous Galerkin method for elastohydrodynamic lubrication line contact problems, Commun. Num. Meth. Engng. 21 (2005) 643–650.

[17] J. Korelc, Multi-language and multi-environment generation of nonlinear finite element codes, Engineering with Computers 18 (2002) 312–327.

[18] N. Patir, H. Cheng, An average flow model for determining effects of three-dimensional roughness on partial hydrodynamic lubrication, Trans. ASME J. Lubr. Technol. 100 (1978) 12–17.